Colloidal AgBiS$_2$ nanocrystals with reduced recombination yield 6.4% power conversion efficiency in solution-processed solar cells

Ignasi Burgués-Ceballos [a], Yongjie Wang [a], M. Zafer Akgul [a], Gerasimos Konstantatos [a,b,*]

[a] *ICFO-Institut de Ciencies Fotòniques, The Barcelona Institute of Science and Technology, 08860, Castelldefels, Barcelona, Spain*
[b] *ICREA-Institució Catalana de Recerca i Estudis Avancats, Passeig Lluís Companys 23, 08010, Barcelona, Spain*

A R T I C L E   I N F O

A B S T R A C T

AgBiS$_2$ nanocrystals have recently emerged as a RoHS compliant material for photovoltaics. This heavy-metal-free ternary chalcogenide can be prepared from earth-abundant precursors, is solution-processable and presents a high absorption coefficient as well as a suitable bandgap for solar cell applications. However, the full potential of AgBiS$_2$ nanocrystals is yet to be realised; the highest efficiencies reported so far used very thin (~35 nm) absorbing layers due to the limited carrier transport and trap-assisted recombination that hinder the performance of thicker layers. In this work we implement a synthetic route to obtain larger size colloidal AgBiS$_2$ nanocrystals, which in turn allows to fabricate thin film solar cells with higher mobility and reduced trap-assisted recombination, resulting in a power conversion efficiency of 6.4%, due to a photocurrent increase of 4 mA/cm^2 compared to prior reports. We conclude by discussing on the main current challenges underpinning the photovoltaic performance of this material as well as strategies to further reduce the voltage and photocurrent losses.

1. Introduction

AgBiS$_2$ nanocrystals (NC) are easy to produce employing low-cost solution processed techniques, and they are based on environmentally friendly elements. They exhibit a high absorption coefficient as well as a suitable bandgap for light harvesting [1]. In addition, the cubic rocksalt AgBiS$_2$ structure (space group, *Fm-3m*) is unlikely to present heavy structural distortions, hence favouring kinetic stability [2]. It is because of all this that AgBiS$_2$ is gaining a lot of attention in the last years amongst heavy-metal-free ternary chalcogenides considered for photovoltaic applications [3]. Several works have reported on synthetic strategies to obtain AgBiS$_2$ nanocrystals of different sizes and shapes [4–8] as well as on their processing and film formation [9,10]. The potential of this material has been demonstrated in solution-processed solar cells using very thin photoactive layers (~35 nm) [11]. Importantly, those devices were fabricated under ambient conditions at low temperatures (≤100 °C). However, the short-circuit current density (J_{sc}) values under 1 sun illumination decreased when using thicker absorber films. Poor carrier transport and Shockley–Read–Hall (SRH) trap-assisted recombination were responsible for incomplete charge extraction before recombination [12,13]. We hypothesized that the

origin of recombination in this material as well as its limited carrier diffusion length lies on surface trap states. Thus we posited that by minimizing the surface to volume ratio via using larger sized nanocrystals would lead to an improvement in carrier transport and charge collection efficiency. In this work we show a modified synthetic approach that yields colloidal AgBiS$_2$ nanocrystals with increased average size, compared to prior art [11], which indeed improve the charge transport balance and consequently the photovoltaic performance in thin film solar cells.

2. Results and discussion

2.1. Double-step hot-injection synthesis of AgBiS$_2$ nanocrystals

With the aim of obtaining colloidal AgBiS$_2$ nanocrystals with a larger average size, we have modified our previously reported, low-temperature hot-injection synthetic route [11]. Instead of injecting the stoichiometric sulfur precursor at once, we perform a sequential, double-step hot-injection approach. First, a small amount (10 % wt.) of the sulfur precursor is injected, which provides the seeds that trigger the nucleation. After a few minutes, the remaining sulfur precursor is added

---

dropwise at a low injection rate in order to favour the growth of larger nanocrystals (see experimental details in ESI†). This method results in a pronounced increase of the average nanocrystal diameter, from 4.3 ± 1.3 nm to 6.5 ± 3.6 nm for the standard (single-injection) and modified (double-injection) syntheses, respectively (Fig. 1). The presence of multiple domains in the larger particles suggests a coalescent crystal growth. Since there is no quantum confinement in this range of crystal dimensions, the broader size distribution observed using this synthetic method does not have a negative impact in the performance of solar cell devices.

On the other hand, the high-resolution transmission electron microscopy (HR-TEM) image and fast Fourier transform (FFT) analysis of a large (~11 nm diameter) nanocrystal (Fig. S1 Supporting Information) reveal no changes in the atomic planes nor in the d-space values with respect to the previously reported nanocrystals from the single-injection synthesis: the observed 3.32 Å (111), 2.90 Å (200) and 2.04 Å (220) interplanar distances (lattice planes) correspond to the cubic rock salt structure. In good agreement, the XRD data (Fig. S2) prove that the crystal structure remains unchanged. The analysis of the peaks corresponding to those three lattice planes corroborates the increase of the average crystallite size, from 3.8 ± 0.2 nm to 5.4 ± 0.1 nm. These values match very well with the median values of the lognormal distribution of particle size determined from the TEM measurements, which were found to be of 4.0 nm and 5.1 nm, respectively. The XPS spectra also confirm the preserved stoichiometry (Fig. S3).

2.2. Impact of nanocrystal size on photovoltaic performance

Inverted structure solar cells were built using either small or larger $AgBiS_2$ nanocrystals in order to evaluate any influence of the enlarged nanocrystal size. The optimised device stack, developed previously in our group [11], and the approximate energy levels are displayed in Fig. 2a and b, respectively. These solar cells were processed in air at room temperature, using mild annealing conditions (see experimental details). The absorber layers were prepared by means of a layer-by-layer deposition process [14], in which the insulating oleate capping ligands that allow the colloidal stability of $AgBiS_2$ nanocrystals in organic solvents are exchanged with inorganic halide ions. In particular, our previous results proved that treating the as-deposited layers with tetramethylammonium iodide (TMAI) resulted in a better passivation of the surface [11]. Additionally, it was also demonstrated that the inclusion of an ultrathin, thiophene-rich polymer layer as an electron-blocking layer facilitates hole extraction from the $AgBiS_2$ layer, thus improving charge collection, albeit not contributing significantly to carrier generation.

The results of the best solar cell devices show a significant improvement in the power conversion efficiency (PCE), from 5.61% for the control device to 6.37% for that using the larger nanocrystals (see Table 1 and Fig. 2c). The modified method results in a +4 mA cm^{-2} increase in the short-circuit current density (J_{sc}) under 1 sun illumination. In contrast, the integrated external quantum efficiency (EQE) spectra (Fig. 2d) do not show such a large difference in J_{sc} (+1.5 mA

cm^{-2}) between the two samples. The reason for this mismatch is related to the higher intensity-dependent current loss in the small nanocrystals, as will be discussed later in the text. We note that the extended absorption tail seen in the EQE spectra as well as the absence of photoluminescence in $AgBiS_2$ are related to the nature of its bandgap. Previous theoretical studies predict that bulk matildite $AgBiS_2$ (cubic rocksalt) structure possesses an indirect gap, as well as a very high dielectric constant and absorption coefficient [15]. On the other hand, neither the fill factor (FF) nor the open-circuit voltage (V_{oc}) suffer meaningful variations. Yet, we investigated the origin of the small drop in V_{OC} upon NC size increase. First, we studied the morphology and band levels of the two systems and observed none or marginal differences between them (Figs. S5 and S6), precluding therefore their role as determinant factors of the small changes in V_{OC} measured therein. Instead, that variation can be explained when combining the changes in the absorption onset and the voltage losses, which is discussed in detail in the next section.

According to our transfer-matrix model simulations, $AgBiS_2$ solar cells could theoretically deliver even higher J_{sc} values (>27 mA cm^{-2}) with thicker absorbing layers, close to 200 nm. The experimental results (Fig. 2e), however, do not follow the predicted trend: the measured J_{sc} at 1 sun drop off at high thicknesses, suggesting a decreasing current collection efficiency in these conditions. Noteworthy, this mismatch is less severe in the larger nanocrystals. For instance, at a thickness of 220 nm the J_{sc} drops down to 7.3 mA cm^{-2} for the reference device whereas the larger nanocrystal devices still provide 17.3 mA cm^{-2}.

To investigate on the origin of this improvement, we determined the current collection efficiency of these two thick devices from bias-dependent EQE measurements [16]. More details are shown in Fig. S7. The results, plotted in Fig. 2f, confirm an appreciable enhancement in the voltage-dependent photocurrent collection for the larger nanocrystals. On the other hand, the reference device suffers a more dramatic drop in photocurrent collection even at low bias.

To verify our hypothesis that larger sized NCs cater for higher carrier mobility, we fabricated hole-only and electron-only devices to measure the single-carrier mobility in the space-charge-limited current (SCLC) regime, as it is arguably a convenient method for investigating charge transport properties of semiconductors [17–19]. While the electron mobility barely changed from small to large nanocrystals, the hole mobility increased almost by an order of magnitude (see Table 1). Moreover, this resulted in a much more balanced hole-electron mobility (1:5 to 2.2:1). To further elucidate the role of the NC size on the recombination processes, we conducted the following investigations: First, the diode ideality factor was calculated from the logarithmic fit to the dependence of V_{oc} on light intensity (Fig. 3a). The fit gives an ideality factor of 1.56 and 1.21 for the small and large NCs, respectively, which indicates suppression of Shockley–Read–Hall (SRH) trap-assisted recombination [20]. In parallel, the change of J_{SC} with light intensity shows less abrupt trends (Fig. 3b). The power-law fit ($J_{SC} \propto$ intensity$^\alpha$) gives an α value of 0.93 and 0.95 for the small and large nanocrystals, respectively. However, these data reveal that J_{SC} at high light intensities is lower for the small NCs, while such difference is not visible at low light intensities comparing the two samples. This intensity-dependent current loss is related to the dissimilar recombination dynamics and is the reason for the mismatch in the difference in J_{SC} measured from the J-V curves at 1 sun (Fig. 2c) in contrast to that extracted from the integrated EQE spectra (Fig. 2d), measured at significantly lower light intensities. Finally, the average carrier lifetimes τ were determined as a function of V_{OC} by fitting transient photovoltage (TPV) decays under light intensities ranging from 0.1 sun to 1 sun. The carrier lifetimes follow the expected trend [21], as they decrease with increasing V_{OC} (and light intensity) for both the small and large NCs samples (Fig. 3c). The latter clearly show, however, a longer lifetime: at 1 sun the carrier lifetime jumps from 1.9 μs to 3.2 μs. These data were combined with those from transient photocurrent (TPC) measurements and we found that the midgap trap state density decreases more than one order of magnitude, from ~$2.8 \cdot 10^{19}$ cm^{-3} eV^{-1} to ~$1.5 \cdot 10^{18}$ cm^{-3} eV^{-1} (Fig. S8) when using
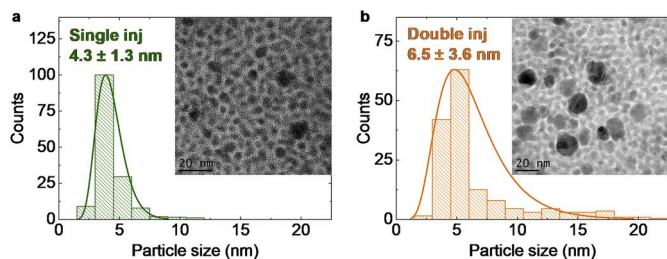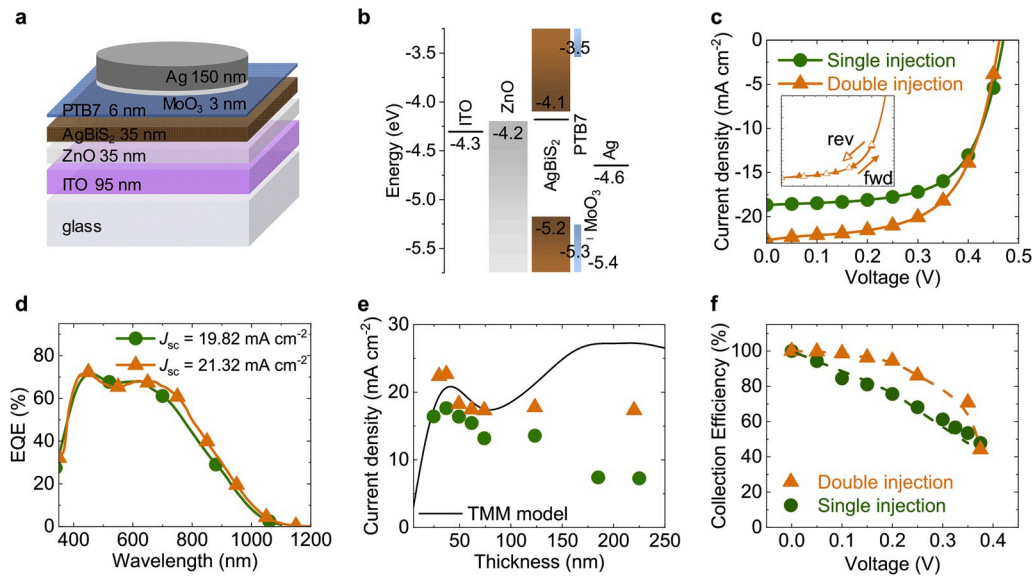

Fig. 1. Particle size distribution resulting from the (a) single-step and (b) double-step hot-injection synthetic approaches. Insets show TEM images of the corresponding $AgBiS_2$ nanocrystals.

Fig. 2. (a) Optimised AgBiS$_2$ solar cell stack and (b) approximate energy level diagram. Comparison of the best solar cell devices using small (green dots) and large (orange triangles) nanocrystals: (c) J-V curves (inset demonstrates absence of hysteresis), (d) external quantum efficiency, (e) J_{SC} values extracted from the integrated EQE spectra as a function of AgBiS$_2$ layer thickness, overlapped with TMM simulation (line) and (f) Charge collection efficiency of thick devices (~220 nm) extracted from bias-dependent EQE. (For interpretation of the references to colour in this figure legend, the reader is referred to the Web version of this article.)

Table 1
Summary of the best device performance parameters and mobility (from SCLC devices). Statistical data is shown in brackets (see also Fig. S4).

| AgBiS$_2$	PCE (%)	FF	V_{oc} (V)	J_{sc} (mA cm^{-2})	J_{sc}.[a](mA cm^{-2})	μ_{h+} (cm^2 V^{-1} s^{-1})	μ_{e-} (cm^2 V^{-1} s^{-1})	μ_{h+}: μ_{e-}
single-injection	5.61 (5.41 ± 0.11)	0.64 (0.63 ± 0.02)	0.47 (0.48 ± 0.01)	18.65 (18.02 ± 0.49)	19.82	2.2 ·10^{-6} ± 2·10^{-7}	1.0·10^{-5} ± 2·10^{-6}	1 : 5
double-injection	6.37 (6.02 ± 0.23)	0.61 (0.61 ± 0.02)	0.46 (0.46 ± 0.01)	22.68 (21.18 ± 0.87)	21.32	1.6 ·10^{-5} ± 9·10^{-7}	7.3 ·10^{-6} ± 2·10^{-6}	2.2 : 1

[a] Integrated from EQE spectra.
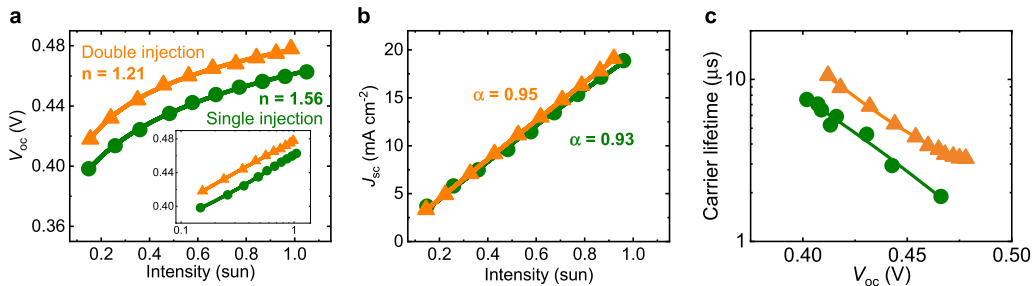
Fig. 3. Optoelectronic characterisation of AgBiS$_2$ solar cells from small (green dots) and large (orange triangles) nanocrystals: (a) V_{OC} as a function of light intensity and the logarithmic fit used to determine the ideality factor n; $V_{OC} \approx \frac{nkT}{q}\ln(\Phi)$, where kT is the thermal energy and q is the elementary charge, (b) J_{SC} as a function of light intensity and the power-law fit ($J_{sc} \propto$ intensity$^{\alpha}$) and (c) carrier lifetimes extracted from transient photovoltage (TPV) measurements as a function of V_{OC}, with the corresponding exponential fit (lines). (For interpretation of the references to colour in this figure legend, the reader is referred to the Web version of this article.)

the large nanocrystals. We conclude that the observed improvement in photocurrent is directly related to the presence of lower midgap trap-state density [22].

2.3. Current limitations in AgBiS$_2$ nanocrystal solar cells

The results reported in this work point at the moderate mobility of AgBiS$_2$ nanocrystals in their current state as one of the factors that limit the performance of solar cells. This negative effect is obviously more evident with increasing active layer thickness. On the other hand, temperature can greatly influence charge transport, especially in low-mobility semiconductors [23]. To understand to which extent this parameter influences our devices, we carried out

temperature-dependent studies. Very clear trends can be seen in the parameters extracted from T-dependent J-V characteristics at 1 sun (Fig. 4), similar to other works on PbS quantum dot solar cells [24–26] (J-V curves are provided in Fig. S9). Excluding the values below 200 K, with increasing temperature there is a simultaneous linear decay of the V_{OC} (−1.8 mV/°C) and a logarithmic growth of the J_{SC}; the FF increases linearly with temperature until 280 K and then plateaus. As a result of this trade-off the PCE reaches its maximum at a temperature of 270 K. The trends of both the J_{sc} and FF can be explained in regards of charge carrier mobility; at low temperature the reduced mobility becomes the major limiting factor, as it hampers carrier extraction and facilitates recombination. This is also confirmed with the dramatic increase of the series resistance in the T-dependent J-V characteristics in dark
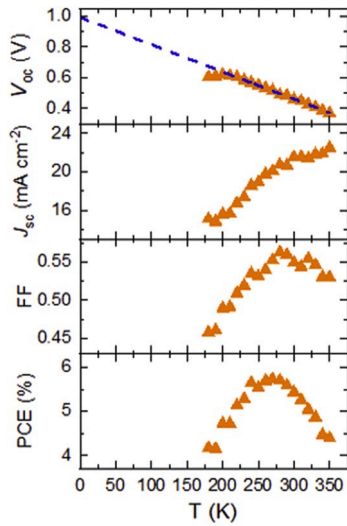
Fig. 4. Temperature-dependent performance parameters extracted from the *J-V* characteristics under 1 sun. The dashed line shows the extrapolation of the dependence of the V_{OC} with temperature in the linear regime, giving a V_{OC} of ~1 V at 0 K.

conditions (Fig. S9). On the other hand, the parallel resistance appears to have a lower impact. Additionally, the increase of the dark ideality factor, even beyond a value of 2 for T < 240 K, indicates that trap-assisted recombination greatly dominates at low temperatures, where energy is insufficient to promote charge de-trapping. The saturation dark current density (J_0), extracted from the Shockley diode equation [27], also follows the expected trend, as it decreases with decreasing T in the whole temperature range [28].

V_{OC} temperature dependence can additionally provide further insights on the determinant factors of open circuit voltage in solar cells. At room temperature the value of the V_{OC} (0.461 V) is significantly lower than the optical energy gap, E_g (1.11 eV, determined from the onset of the external quantum efficiency). The extrapolation of the dependence of the V_{OC} with temperature in the linear regime (dashed line in Fig. 4), however, yields a value of ~1 V at 0 K (that is, with zero losses due to thermalisation), very close to the semiconductor bandgap. This indicates the absence of interface loss effects on the limited V_{OC} at room temperature and points to the presence of trap assisted recombination. It is therefore interesting to analyse and quantify the energy losses in order to understand in more detail their nature and thus estimate the real potential of AgBiS$_2$ nanocrystals solar cells (Fig. 5). In order to evaluate the different contributions to the loss in open-circuit voltage we used a method based on the detailed balance theory and the reciprocity relation between light absorption and light emission [29,30].

First, we determined a value of 0.868 V for the open-circuit voltage in the Shockley-Queisser limit [31], $V_{OC,SQ}$, assuming a step-function-like quantum efficiency and radiative recombination only [32]:

$$V_{OC,\ SQ} = \frac{k_B T}{q} ln\left(\frac{J_{SC,\ SQ}}{J_{0,\ SQ}} + 1\right) \cong \frac{k_B T}{q} ln\left(\frac{q \int_{E_g}^{+\infty} \varnothing_{AM1.5G}(E)dE}{q \int_{E_g}^{+\infty} \varnothing_{BB}(E)dE}\right) \quad (1)$$

Here, k_B is the Boltzmann constant, T is the temperature of the solar cell, q is the elementary charge, and $\varnothing_{AM1.5G}(E)$ and $\varnothing_{BB}(E)$ are the standard solar AM1.5G and the black body spectra, respectively. Consequently, $J_{SC,SQ}$ corresponds to the short-circuit current density in the SQ limit, obtained from the integral of the ideal step-function EQE spectrum, whereas $J_{0,SQ}$ is the radiative limit of the dark current, obtained by integrating the product of the EQE and the black body spectra at room temperature. The first voltage losses, $E_{g,opt}/q - V_{OC,SQ}$, equal 0.242 V, matching the typical values of other photovoltaic materials
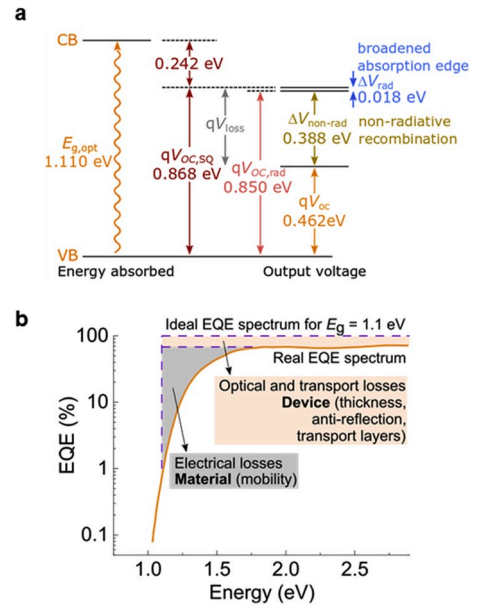
Fig. 5. (a) Estimation of voltage losses qV_{loss}, considering the energy bandgap E_g, the output voltage qV_{OC} and the calculated V_{OC} at the Shockley-Queisser limit q$V_{OC,SQ}$, and at the radiative limit q$V_{OC,\ rad}$. (b) Comparison of the real and an ideal step-wise EQE spectra to illustrate how optical and electrical losses also result in photocurrent losses. Improved material properties (mobility) would sharpen the absorption edge, while transport properties of the device as well as light management can also help maximise the output photocurrent of solar cells.

[30]. These losses are unavoidable, as they are fundamentally related to the absorption of light [33]. Therefore, we exclude them from the V_{loss} term.

Then, we used the real EQE spectrum to calculate the open-circuit voltage at the radiative limit $V_{oc,rad}$ [32], that is, assuming that all the absorbed photons would only be emitted radiatively (absence of thermalisation) and obtained a value of 0.850 V

$$V_{OC,\ rad} = \frac{k_B T}{q} ln\left(\frac{J_{SC}}{J_{0,rad}} + 1\right) \cong \frac{k_B T}{q} ln\left(\frac{q \int_0^{+\infty} \varnothing_{AM1.5G}(E)dE}{q \int_0^{+\infty} \varnothing_{BB}(E)dE}\right) \quad (2)$$

The second voltage losses, $\Delta V_{OC,abs}$, determined from the difference between $V_{OC,SQ}$ and $V_{OC,rad}$, account for the red shift of the emission relative to the broadened absorption edge [34]. In our material these losses were found to be of 0.018 V. Although low, this value is one order of magnitude higher than the typical ΔV_{rad} losses observed in other inorganic semiconductors such as c-Si, CIGS, GaAs or lead iodide based perovskites [35–37], suggesting a higher disorder in our AgBiS$_2$ nanocrystals, due to (surface) defects that may cause the creation of band tails of localised states [35]. In the case of amorphous Si, for instance, Kirchartz et al. ascribed the observed deviations in the reciprocity relation between quantum efficiency and electroluminescence (EL) to the presence of localised mid-gap states due to dangling bonds as well as to the red-shift to the EL from tail-to-tail transitions (Stokes shift) [38]. Unfortunately, we could not conduct such studies in our AgBiS$_2$ nanocrystals, as they do not show photoluminescence at room temperature.

Thirdly, from the difference between $V_{OC,rad}$ and the real V_{OC} we estimated that the losses due to non-radiative recombination, $\Delta V_{non-rad}$, correspond to 0.388 V. This is by far the highest contribution to voltage losses in our AgBiS$_2$ system and is significantly higher compared with other inorganic solar cells, which show non-radiative losses in the range of 0.04–0.21 V [30]. Further increasing the mobility or reducing the number of impurities and defects that act as recombination centres would decrease these losses.

The comparison of these losses with those of the reference device

(Table S1) reveals a moderate decrease of 11 mV in voltage losses: the radiative losses drop from 22 mV to 18 mV and the non-radiative losses drop from 395 mV to 388 mV. On the other hand, the increase of the NC size resulted in a red-shift of 18 meV in the optical bandgap (from 1.128 eV to 1.110 eV). In perfect agreement with these values, the experimental V_{OC} data present a difference of 7 mV (from 0.469 V to 0.462 V), which match with the lost 18 mV due to the bandgap and the gained 11 mV from the voltage losses.

In addition to the voltage losses, we reckon significant losses in the extracted photocurrent (Fig. 5b). On the one hand, the EQE spectrum exhibits a shallow absorption edge. The modest steepness in the low-energy tail compared with the ideal step-wise EQE spectrum implies energy losses not only in voltage but also in photocurrent. The shallow absorption edge induces low EQE for photons with energy just above the energy bandagp [39]. For a steep absorption edge, this photocurrent loss would be minimised. We believe that a deeper understanding and a stronger control of the surface composition of the ternary $AgBiS_2$ nanocrystals would be of great importance to mitigate these defect-derived losses.

Finally, the last source of photocurrent losses relates to optical and transport losses, which prevent the solar cells from achieving the maximum obtainable EQE. As we have discussed in the previous section, the moderately low mobility of this system still hampers the extraction of photocurrent in solar cells with $AgBiS_2$ layers thicker than ~50 nm, consequently limiting the light harvesting capability of these devices.

3. Conclusions

We have implemented a modified synthetic method, based on a double-step hot-injection approach, to obtain ternary $AgBiS_2$ nano-crystals with a significant increase in the average diameter (6.5 ± 3.6 nm) compared with our previous process (4.3 ± 1.3 nm). The resulting nanocrystals preserve the crystal structure and stoichiometry. As a direct consequence of the enhanced average size, the photocurrent of solution-processed solar cells using these nanocrystals increases by 4 mA/cm², and the power conversion efficiency increases from 5.6% to 6.4%. We conclude that the newly developed nanocrystals induce an improved hole mobility and subsequent better hole:electron mobility balance, a reduced recombination and a lower midgap trap state density. Yet, further improvements are needed to exploit the full potential of this material. Our studies on the energy losses suggest that a higher mobility and a lower density of impurities and defects are essential to minimise losses in voltage and the extracted photocurrent. We speculate that further increasing the nanocrystal size could enhance even more the mobility as well as decrease recombination. In order to reduce the number of defects, on the other hand, we first advocate a deeper understanding of the composition and stoichiometry of the nanocrystal surface as well as encourage more advanced approaches such as single-step deposition or solution-phase ligand exchange processes that help reduce the number of induced impurities.

4. Experimental section

4.1. Materials

All the reagents were purchased from Sigma Aldrich, except for Bi $(OAc)_3$, which was purchased from Alfa Aesar. Poly[[4,8-bis[(2-ethyl-hexyl)oxy]benzo[1,2-b:4,5-b']dithiophene-2,6-diyl][3-fluoro-2-[(2-eth-ylhexyl)carbonyl]thieno[3,4-b]thiophenediyl]] (PTB7) was purchased from 1-Material. The ITO-covered glass substrates were acquired from the Institut für Großflächige Mikroelektronik, Universität Stuttgart.

4.2. Synthesis of $AgBiS_2$ nanocrystals

All the reactions were carried out using standard Schlenk techniques. For the control synthesis we followed our previously reported, low-temperature hot-injection synthetic route [11]. In brief, 1 mmol Bi $(OAc)_3$, 0.8 mmol Ag(OAc) and 17 mmol oleic acid (OA) were pumped overnight at 100 °C to form the Bi and Ag oleates and remove oxygen and moisture. After that, the reaction atmosphere was switched to Ar, to quickly inject 1 mmol hexamethyldisilathiane (HMS) dissolved in 5 ml 1-octadecene (ODE) under vigorous stirring. The heating was stopped, without removing the heating mantel, and the reaction was allowed to cool down slowly. Upon addition of acetone and centrifugation, the nanocrystals were isolated and purified by successive dispersion in toluene and precipitation with acetone. The oleic-capped colloidal nanocrystals were finally dispersed in anhydrous toluene and 0.45 μm polytetrafluoroethylene (PTFE) filtered. In the sequential, double in-jection synthetic approach we kept the stoichiometric amounts un-changed and followed exactly the same steps, except for the addition of the sulfur precursor: first, 0.1 mmol HMS were quickly injected. After 3 min and without removing the heating, the remaining 0.9 mmol HMS were added dropwise at a rate of 0.3 mL min⁻¹. The heating was removed once all the sulfur precursor was added.

4.3. Characterisation of $AgBiS_2$ nanocrystals

TEM and XRD measurements were performed at the Scientific and Technological Centres of the University of Barcelona (CCiT-UB). TEM micrographs were obtained using a JEOL 2100 microscope operating at an accelerating voltage of 200 kV. The samples were prepared by placing one drop of a diluted toluene solution on a holey carbon-coated grid and allowing the solvent to evaporate in air. The average diameter was calculated by measuring the diameters of ~200 nanocrystals from non-aggregated areas. XRD data were collected using a PANalytical X'Pert PRO MPD Alpha1 powder diffractometer in Bragg–Brentano θ/2θ ge-ometry with a radius of 240 mm, Cu Kα radiation (λ = 1.5406 Å) and a power of 45 kV–40 mA.

UPS and XPS measurements were performed at the Institut Català de Nanociencia i Nanotecnologia (ICN2). XPS measurements were per-formed with a Phoibos 150 analyser (SPECS) in ultrahigh-vacuum con-ditions (base pressure of 1 × 10–10 mbar) with a monochromatic Kα X-ray source (1486.74 eV). Accurate binding energies (0.2 eV) were determined by referencing to the C 1s peak at 284.8 eV. UPS measure-ments were performed on a SPECS PHOIBOS 150 electron spectrometer using monochromated HeI radiation (21.2 eV). For the latter, the sam-ples were prepared by covering ITO substrates (~10 × 10 mm²) with concentrated $AgBiS_2$ toluene-based solutions and allowing the solvent to evaporate in air.

4.4. Fabrication of solar cells

ITO-covered glass substrates were cleaned by sequential ultra-sonication in soapy water, acetone and isopropanol for 10 min each and dried with nitrogen. A sol-gel method was used to grow a ~35 nm ZnO layer on top of ITO. Zinc acetate dehydrate (500 mg) was dissolved in 5 ml methoxyethanol and 142 μl ethanolamine. The solution was 0.2 μm polyvinylidene difluoride (PVDF) filtered, spin-cast onto the ITO-covered glass substrates at 3000 rpm and heated at 250 °C for 30 min. This process was performed twice to achieve a uniform film coverage. Then, a layer-by- layer (LbL) process was followed to deposit the $AgBiS_2$ films. Each LbL step consisted of i) casting one drop of 20 mg ml⁻¹ so-lution of $AgBiS_2$ in toluene onto the ZnO at a spinning speed of 2000 rpm and waiting 10 s, ii) adding 5 drops of tetramethylammonium iodide (TMAI, 1 mg ml⁻¹ in methanol) and waiting 20 s, iii) repeating step ii, iv) rinsing with methanol and then with toluene. To modify the thick-ness of the absorbing layer, the number of LbL steps was changed from 1 to 15. For the record devices the optimum thickness was set to ~35 nm, corresponding to 3 LbL. After the deposition of $AgBiS_2$, the samples were annealed for 10 min at 100 °C in air and then stored in the dark over-night. Then, a thin (~6 nm) layer of PTB7 was spin cast at 2000 rpm from a 5 mg ml⁻¹ solution in o-Dichlorobenzene. Finally 3 nm of MoO_3

and 150 nm of Ag were sequentially evaporated through a shadow mask (2 mm diameter, 3.1 mm^2 area) in a Kurt J. Lesker Nano36 system.

4.5. Characterisation of solar cells

The current–voltage measurements were performed with a Keithley 2400 source meter and a calibrated Newport Oriel Sol3A solar simulator (AM 1.5 G) under ambient conditions. The EQE and bias-dependent EQE were measured using a Newport Cornerstone 260 monochromator, a Thorlabs MC2000 chopper, a Stanford Research SR570 trans-impedance amplifier and a Stanford Research SR830 lock-in amplifier. A calibrated Newport 818-UV photodetector was used as a reference. The light intensity dependence of V_{SC} and J_{SC} was measured with a FiberTech Optic LED light source calibrated with a Newport 818-UV power meter and an Agilent 4000X oscilloscope. The intensity of the lamp was varied with the DC applied bias from the function generator of the oscilloscope. The voltage (current) was acquired on the oscilloscope with an input impedance of 1 MΩ (50 Ω).

Space-charge-limited current (SCLC) measurements were performed in single-carrier devices in order to determine the hole and electron mobilities, using the Mott-Gurney [40] law $J = \frac{9}{8}\mu\varepsilon_0\varepsilon_r\,_{AgBiS_2}\frac{V^2}{L^3}$. The device structure for the hole-only (electron-only) device was ITO/PEDOT: PSS/AgBiS$_2$/MoO$_3$/Ag (ITO/ZnO/AgBiS$_2$/LiF/Al), with an active layer thickness of 420 nm. The fitting was done in the regime where the slope $m = \frac{dlogJ}{dlogV}$ has a value of 2 [19].

Transient photovoltage, TPV, (transient photocurrent, TPC) measurements were performed with an Agilent 4000X oscilloscope using a 1MΩ (50 Ω) input terminal and a Vortran Stradus laser with a wavelength of 637 nm. A FiberTech Optica LED light source provided the bias light. A function generator was used to control the laser, with a frequency of 10 Hz and pulse width of 100 μs. The intensity of the laser was adjusted to keep the voltage transient amplitude under 5% of the steady state light bias. Carrier lifetime τ and V_{OC} were determined by fitting the exponential photovoltage decays with $V = A\,e^{\left(\frac{-t}{\tau}\right)} + V_{OC}$, where V is the photovoltage, A is an exponential prefactor and t is time. The trap state density was calculated by combining the TPV and TPC data [21, 22].

Simultaneous temperature and light-dependent J-V measurements were performed in a Lakeshore four-probe cryogenic chamber controlled by a Lakeshore-360 module and an Abet 10500 solar simulator equipped with a Thorlabs neutral density filter wheel. The photovoltaic parameters were obtained using a Keysight B1500A device analyser in a range of temperatures between 180 K and 350 K and light intensities between 0.1 suns and 1 sun. The dark ideality factor n and the dark saturation current J_0 were calculated by fitting the diode equation in the linear regime of the semilog J-V curves in dark conditions, where series and parallel resistance have a negligible impact: $J = J_0\left(e^{\frac{qV}{nkT}} - 1\right)$.

Declaration of competing interest

The authors declare that they have no known competing financial interests or personal relationships that could have appeared to influence the work reported in this paper.

CRediT authorship contribution statement

Ignasi Burgués-Ceballos: Conceptualization, Investigation, Writing - original draft. **Yongjie Wang:** Investigation. **M. Zafer Akgul:** Investigation. **Gerasimos Konstantatos:** Conceptualization, Supervision, Writing - original draft.

Appendix A. Supplementary data

Supplementary data to this article can be found online at https://doi.org/10.1016/j.nanoen.2020.104961.

References

[1] B. Pejova, D. Nesheva, Z. Aneva, A. Petrova, Photoconductivity and relaxation dynamics in sonochemically synthesized assemblies of AgBiS2 quantum dots, J. Phys. Chem. C 115 (2011) 37–46, https://doi.org/10.1021/jp106605t.

[2] S.N. Guin, K. Biswas, Cation disorder and bond anharmonicity optimize the thermoelectric properties in kinetically stabilized rocksalt AgBiS2 nanocrystals, Chem. Mater. 25 (2013) 3225–3231.

[3] N.C. Miller, M. Bernechea, Research Update: bismuth based materials for photovoltaics, Apl. Mater. 6 (2018), 084503, https://doi.org/10.1063/1.5026541.

[4] C. Chen, X. Qiu, S. Ji, C. Jia, C. Ye, Synthesis of monodispersed AgBiS2 quantum dots with a giant dielectric constant, CrystEngComm 15 (2013) 7644–7648, https://doi.org/10.1039/b000000x.

[5] P. Huang, W. Yang, M. Lee, AgBiS2 semiconductor-sensitized solar cells, J. Phys. Chem. C 117 (2013) 18308–18314.

[6] N. Liang, W. Chen, F. Dai, X. Wu, W. Zhang, Z. Li, et al., Homogenously hexagonal prismatic AgBiS2 nanocrystals: controlled synthesis and application in quantum dot-sensitized solar cells, CrystEngComm 17 (2015) 1902–1905, https://doi.org/10.1039/C4CE02405B.

[7] S. Zhou, J. Yang, W. Li, Q. Jiang, Y. Luo, D. Zhang, et al., Preparation and photovoltaic properties of ternary AgBiS 2 quantum dots sensitized TiO 2 nanorods photoanodes by electrochemical atomic layer deposition, J. Electrochem. Soc. 163 (2016) D63–D67, https://doi.org/10.1149/2.0161603jes.

[8] L. Hu, Robert.J. Patterson, Z. Zhang, Y. Hu, D. Li, Z. Chen, et al., Enhanced optoelectronic performance in AgBiS2 nanocrystals from an improved amine-based synthesis route, J. Mater. Chem. C. 6 (2018) 731–737, https://doi.org/10.1039/C7TC05366E.

[9] N. Pai, J. Lu, D.C. Senevirathna, A.S.R. Chesman, T. Gengenbach, M. Chatti, et al., Spray deposition of AgBiS2 and Cu3BiS3 thin films for photovoltaic applications, J. Mater. Chem. C. 6 (2018) 2483–2494, https://doi.org/10.1039/C7TC05711C.

[10] E. Gu, X. Lin, X. Tang, G.J. Matt, A. Osvet, Y. Hou, et al., Single molecular precursor ink for AgBiS2 thin films: synthesis and characterization, J. Mater. Chem. C. 6 (2018) 7642–7651, https://doi.org/10.1039/c8tc01195h.

[11] M. Bernechea, N.C. Miller, G. Xercavins, D. So, A. Stavrinadis, G. Konstantatos, Solution-processed solar cells based on environmentally friendly AgBiS2 nanocrystals, Nat. Photon. 10 (2016) 521–525, https://doi.org/10.1038/nphoton.2016.108.

[12] T. Kirchartz, F. Deledalle, P.S. Tuladhar, J.R. Durrant, J. Nelson, On the differences between dark and light ideality factor in polymer:Fullerene solar cells, J. Phys. Chem. Lett. 4 (2013) 2371–2376, https://doi.org/10.1021/jz4012146.

[13] S.R. Cowan, A. Roy, A.J. Heeger, Recombination in polymer-fullerene bulk heterojunction solar cells, Phys. Rev. B Condens. Matter 82 (2010) 1–10, https://doi.org/10.1103/PhysRevB.82.245207.

[14] R. Wang, Y. Shang, P. Kanjanaboos, W. Zhou, Z. Ning, E.H. Sargent, Colloidal quantum dot ligand engineering for high performance solar cells, Energy Environ. Sci. 9 (2016) 1130–1143, https://doi.org/10.1039/C5EE03887A.

[15] F. Viñes, M. Bernechea, G. Konstantatos, F. Illas, Matildite versus schapbachite: first-principles investigation of the origin of photoactivity in AgBiS2, Phys. Rev. B 94 (2016) 235203, https://doi.org/10.1103/PhysRevB.94.235203.

[16] C.J. Hages, N.J. Carter, R. Agrawal, Generalized quantum efficiency analysis for non-ideal solar cells: case of Cu2ZnSnSe4, J. Appl. Phys. 119 (2016), 014505, https://doi.org/10.1063/1.4939487.

[17] R.W. Smith, A. Rose, Space-charge-limited currents in single crystals of cadmium sulfide, Phys. Rev. 97 (1955) 1531–1537, https://doi.org/10.1103/PhysRev.97.1531.

[18] R. Steyrleuthner, M. Schubert, F. Jaiser, J.C. Blakesley, Z. Chen, A. Facchetti, et al., Bulk electron transport and charge injection in a high mobility n-type semiconducting polymer, Adv. Mater. 22 (2010) 2799–2803, https://doi.org/10.1002/adma.201000232.

[19] J.A. Röhr, D. Moia, S.A. Haque, T. Kirchartz, J. Nelson, Exploring the validity and limitations of the Mott-Gurney law for charge-carrier mobility determination of semiconducting thin-films, J. Phys. Condens. Matter 30 (2018), 105901, https://doi.org/10.1088/1361-648X/aaabad.

[20] C.H.M. Chuang, A. Maurano, R.E. Brandt, G.W. Hwang, J. Jean, T. Buonassisi, et al., Open-circuit voltage deficit, radiative sub-bandgap states, and prospects in quantum dot solar cells, Nano Lett. 15 (2015) 3286–3294, https://doi.org/10.1021/acs.nanolett.5b00513.

[21] C.G. Shuttle, B. O'Regan, A.M. Ballantyne, J. Nelson, D.D.C. Bradley, J. De Mello, et al., Experimental determination of the rate law for charge carrier decay in a polythiophene: fullerene solar cell, Appl. Phys. Lett. 92 (2008) 1–4, https://doi.org/10.1063/1.2891871.

[22] A.H. Ip, S.M. Thon, S. Hoogland, O. Voznyy, D. Zhitomirsky, R. Debnath, et al., Hybrid passivated colloidal quantum dot solids, Nat. Nanotechnol. 7 (2012) 577–582, https://doi.org/10.1038/nnano.2012.127.

[23] S.M. Sze, Physics of Semiconductor Devices, second ed., Wiley, New York, 1981.

[24] M.J. Speirs, D.N. Dirin, M. Abdu-Aguye, D.M. Balazs, M.V. Kovalenko, M.A. Loi, Temperature dependent behaviour of lead sulfide quantum dot solar cells and films, Energy Environ. Sci. 9 (2016) 2916–2924, https://doi.org/10.1039/c6ee01577h.

[25] Z. Jin, A. Wang, Q. Zhou, Y. Wang, J. Wang, Detecting trap states in planar PbS colloidal quantum dot solar cells, Sci. Rep. 6 (2016) 1–9, https://doi.org/10.1038/srep37106.

[26] A.K. Rath, F.P.G. De Arquer, A. Stavrinadis, T. Lasanta, M. Bernechea, S.L. Diedenhofen, et al., Remote trap passivation in colloidal quantum dot bulk nano-heterojunctions and its effect in solution-processed solar cells, Adv. Mater. 26 (2014) 4741–4747, https://doi.org/10.1002/adma.201400297.

[27] D. Bozyigit, W.M.M. Lin, N. Yazdani, O. Yarema, V. Wood, A quantitative model for charge carrier transport, trapping and recombination in nanocrystal-based solar cells, Nat. Commun. 6 (2015) 6180, https://doi.org/10.1038/ncomms7180.

[28] P.E. Keivanidis, T.M. Clarke, S. Lilliu, T. Agostinelli, J.E. Macdonald, J.R. Durrant, et al., Dependence of charge separation efficiency on film microstructure in poly(3-hexylthiophene-2,5-diyl):[6,6]-phenyl-C61 butyric acid methyl ester blend films, J. Phys. Chem. Lett. 1 (2010) 734–738, https://doi.org/10.1021/jz900296f.

[29] U. Rau, Reciprocity relation between photovoltaic quantum efficiency and electroluminescent emission of solar cells, Phys. Rev. B 76 (2007), 085303, https://doi.org/10.1103/PhysRevB.76.085303.

[30] J. Yao, T. Kirchartz, M.S. Vezie, M.A. Faist, W. Gong, Z. He, et al., Quantifying losses in open-circuit voltage in solution-processable solar cells, Phys. Rev. Appl. 4 (2015), 014020. http://link.aps.org/doi/10.1103/PhysRevApplied.4.014020. (Accessed 4 August 2015).

[31] W. Shockley, H.J. Queisser, Detailed balance limit of efficiency of p-n junction solar cells, J. Appl. Phys. 32 (1961) 510, https://doi.org/10.1063/1.1736034.

[32] Y. Wang, D. Qian, Y. Cui, H. Zhang, J. Hou, K. Vandewal, et al., Optical gaps of organic solar cells as a reference for comparing voltage losses, Adv. Energy Mater. 8 (2018) 1–10, https://doi.org/10.1002/aenm.201801352.

[33] P. Würfel, U. Würfel, Physics of Solar Cells: from Basic Principles to Advanced Concepts, Wiley-VCH Verlag GmbH & Co. KGaA, Weinheim, Germany, 2016.

[34] S.M. Tuladhar, M. Azzouzi, F. Delval, J. Yao, A.A.Y. Guilbert, T. Kirchartz, et al., Low open-circuit voltage loss in solution-processed small-molecule organic solar cells, ACS Energy Lett 1 (2016) 302–308, https://doi.org/10.1021/acsenergylett.6b00162.

[35] T. Kirchartz, U. Rau, M. Kurth, J. Mattheis, J.H. Werner, Comparative study of electroluminescence from Cu(In,Ga)Se2 and Si solar cells, Thin Solid Films 515 (2007) 6238–6242, https://doi.org/10.1016/j.tsf.2006.12.105.

[36] M.A. Green, Radiative efficiency of state-of-the-art photovoltaic cells, Prog. Photovoltaics Res. Appl. 20 (2012) 472–476, https://doi.org/10.1002/pip.

[37] K. Tvingstedt, O. Malinkiewicz, A. Baumann, C. Deibel, H.J. Snaith, V. Dyakonov, et al., Radiative efficiency of lead iodide based perovskite solar cells, Sci. Rep. 4 (2014) 6071, https://doi.org/10.1038/srep06071.

[38] T. Christian, M. Müller, B. Elger, T. Kirchartz, R. Carius, U. Rau, Effect of localized states on the reciprocity between quantum efficiency and electroluminescence in Cu(In,Ga)Se2 and Si thin-film solar cells, Sol. Energy Mater. Sol. Cells 129 (2014) 95–103.

[39] K. Vandewal, J. Benduhn, V.C. Nikolis, How to determine optical gaps and voltage losses in organic photovoltaic materials, Sustain. Energy Fuels. 2 (2018) 538–544, https://doi.org/10.1039/C7SE00601B.

[40] N.F. Mott, R.W. Gurney, Electronic Processes in Ionic Crystals, Oxford University Press, Oxford, 1940.

Dr. Ignasi Burgués-Ceballos is a postdoctoral fellow at the Institute of Photonic Sciences (ICFO), Barcelona. He received his PhD in 2014 from the Institute of Materials Science of Barcelona (ICMAB-CSIC), Autonomous University of Barcelona (UAB), followed by stages as a postdoc at the Cyprus University and Technology and as a research scientist in the OPV physics fundamentals division at Merck Group, Southampton, UK. His research is focused on environmentally friendly materials for solution-processing of hybrid organic-inorganic photovoltaic devices.

Yongjie Wang is a Ph.D student under the supervision of Prof. Gerasimos Konstantatos in the Institute of Photonic Sciences (ICFO), Barcelona, Spain. He graduated from Institute of Functional Nano & Soft Materials (FUNSOM), Soochow University with a master degree in Physics. His research is mainly focused on solution processed nanocrystals for energy harvesting and solar cells.
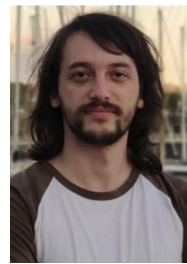
M. Zafer Akgul received his B.S. degree in 2012 and M.S. degree in 2015 from Department of Electrical and Electronics Engineering at Bilkent University. He is currently a Ph.D. candidate at ICFO - The Institute of Photonic Sciences - under the supervision of Prof. Konstantatos. His research is mainly focused on the synthesis and applications of colloidal nanocrystals.

Gerasimos Konstantatos, received his PhD in the department of Electrical and Computer Engineering from the University of Toronto, ON, Canada in 2008. In 2009 he joined ICFO as an assistant Professor and since 2015 he is an ICREA research Professor at ICFO leading the Functional Optoelectronic Nanomaterials Group. His interests lie in developing solution processed nanomaterials, quantum dots and 2D materials for optoelectronic and solar cell applications. He is the recipient of MIT TR35 Spain award in 2012 and Fresnel Prize in 2013 for his salient contributions in the field of colloidal quantum dot optoelectronics.